JOURNAL OF MATERIALS SCIENCE 23 (1988) 1695–1708

Structure and decomposition behaviour of rapidly solidified Al–Cu–Li–Mg–Zr alloys

D. H. KIM, B. CANTOR
Department of Metallurgy and Science of Materials, Oxford University, Oxford, OX1 3PH, UK
H. I. LEE
Korea Advanced Institute of Science and Technology, P.O. Box 131, Chongryang, Seoul, Korea

The microstructural characteristics of Al–Cu–Li–Mg–Zr alloys have been studied after rapid solidification by melt spinning and after subsequent annealing at temperatures in the range 160 to 500° C, by using a combination of optical microscopy, scanning and transmission electron microscopy, X-ray diffraction, differential scanning calorimetry and microhardness measurements. The as-melt-spun alloys consist of a cellular microstructure with fine scale δ' precipitates and icosahedral particles distributed within the cells and at cell boundaries. The icosahedral structure is equivalent to the T_2 phase reported by Hardy and Silcock. Annealing the melt-spun alloys leads to a complex precipitation sequence: $\alpha + I + \delta' \rightarrow \alpha + I + S' + \theta' \rightarrow \alpha + I \rightarrow \alpha + \delta' + T_1 + T_2(\mathrm{bcc})$ + two other phases. The icosahedral particles coarsen progressively during annealing, especially at higher annealing temperatures. Fine-scale δ' precipitates grow during annealing at low temperature, dissolve at higher annealing temperatures below 500° C, and then reprecipitate during cooling after annealing at 500° C. During annealing at low temperature, plates of θ' and S' precipitate and then dissolve, providing solute atoms for icosahedral particle growth. Stable T_1, T_2(bcc) and two other phases precipitate after decomposition of the icosahedral particles during annealing at 500° C.

1. Introduction

Aluminium alloys containing lithium are receiving considerable attention as a potential new generation of aerospace materials, because of their increased moduli and decreased densities compared with other alloys in current use [1–3]. At present the position of aluminium alloys as the main materials for aerospace application is threatened by other advanced materials, and aluminium–lithium alloys are considered to be the best answer to this threat. If these new alloys can be used in existing aircraft designs, then weight savings of 10% can be achieved [4]. However, the introduction of aluminium-lithium alloys has been slowed down by ingot casting difficulties such as the loss of lithium during melting, impurity control, and segregation [5, 6]. Moreover, there is a serious problem of low fracture toughness in the final alloys, because dislocation shear of the strengthening metastable δ' (Al_3Li) precipitates leads to planar slip and strain localization [7, 8].

To overcome ingot casting problems, rapid solidification processing can be used to increase the solubility of alloying and impurity elements, refine the alloy microstructure, and eliminate harmful segregation effects [5]. To solve the toughness problem, slip can be homogenized by adding precipitate-forming elements such as copper and magnesium, and dispersoid-forming elements such as zirconium [9]. Among the alloys which have been investigated so far, the Al–Cu–Li–Mg–Zr alloy system has received most attention because of its balanced combination of strength and ductility [5, 10, 11].

Although some research has been done on aluminium–lithium alloys manufactured by ingot metallurgy and by rapid solidification followed by consolidation, little attention has been given to the as-rapidly solidified structure. Thus, the aim of the present study was to investigate the microstructural characteristics of Al–Cu–Li–Mg–Zr alloys after rapid solidification by melt spinning, and subsequent decomposition behaviour during annealing.

2. Precipitate phases in Al–Cu–Li–Mg–Zr alloys

When an aluminium–lithium alloy is quenched from the single phase region and subsequently aged, decomposition of the supersaturated solid solution occurs by continuous precipitation of δ'(Al_3Li) throughout the matrix [12]. In fact, metastable δ' is usually present even in the as-quenched condition [13, 14]. The δ' phase has a cubic $L1_2$ structure [15], and forms coherently as spherical particles with a cube/cube orientation relationship with the matrix. There is some evidence for the existence of G.P. zones as a precursor to the formation of δ' [16, 17]. After the precipitation of metastable δ', subsequent ageing leads to the formation of the equilibrium δ phase which has a cubic B32 structure [16]. Heterogeneous precipitation of δ occurs preferentially at grain boundaries [18], although Noble and Thomson [14] have also

0022-2461/88 $03.00 + .12

observed plate-like δ in the interiors of grains. The δ phase appears to be absent in aluminium–lithium alloys containing magnesium [19].

The principal phases which can form by reaction of aluminium, copper and lithium atoms are probably T_1, T_B and T_2 which were first reported by Hardy and Silcock [20] in early work on phase equilibria in aluminium-rich ternary Al–Cu–Li alloys. The T_1 phase has a hexagonal crystal structure with an approximate composition of Al_2CuLi, and forms as thin hexagonal-shaped platelets in ternary Al–Cu–Li alloys. The T_1 phase in Al–Cu–Li–Mg alloys is essentially the same as in the ternary alloys, although magnesium can modify the usual hexagonal plate-like morphology of T_1 to a rounded lath [10] or diamond shape [19]. The T_B phase has been reported to have a composition of approximately $Al_{7.5}Cu_4Li$ and a cubic CaF_2 structure [20]. Silcock [15] has suggested that this phase forms from metastable tetragonal $\theta'(Al_2Cu)$ by replacement of aluminium atoms with lithium. The T_2 phase has a composition of Al_6CuLi_3, and has been reported to have either a b c c structure isomorphous with $Mg_{32}(Al, Zn)_{49}$ [21], or an icosahedral structure with $m\bar{3}\bar{5}$ point group symmetry [10, 22, 23]. The icosahedral phase in Al–Cu–Li and Al–Cu–Li–Mg alloys has been observed at grain boundaries in conventionally cast and peak aged or over aged alloys [10, 22–24], and has recently been reported in rapidly solidified Al–Cu–Li–Mg [25]. In addition to T_1, T_B and T_2, Hardy and Silcock have described a stable R phase (Al_5CuLi_3) with a similar composition to T_2, in the Al–Cu–Li system [20].

The existence of metastable T_1' and T_B' phases as precursors of T_1 and T_B was first suggested by Suzuki *et al.* [26]. According to Rioja and Ludwiczak [27], T_1' has an orthorhombic structure and grows continuously to T_1 during annealing. However, Huang and Ardell [28, 29] and Cassada *et al.* [30] have denied the existence of the precursor T_1' phase. Tetragonal $\theta'(Al_2Cu)$ can also form during annealing of Al–Cu–Li alloys [11, 15]. Precipitation of S′ phase is found during ageing of Al–Cu–Li–Mg alloys, with an orthorhombic structure similar to S′ in Al–Cu–Mg alloys. The stable S phase (Al_2CuMg) precipitates after longer ageing times, with a morphology, structure and orientation relationship similar to S′, but with a slightly different lattice parameter [31].

3. Experimental details

3.1. Material

Three different alloys were used in the present study and were prepared by melting and casting high-purity metals in a vacum induction furnace under an argon gas atmosphere. Nominal alloy compositions (wt %) were Al–3Cu–1.5Li–1Mg, Al–3Cu–1.5Li–1Mg–0.1Zr and Al–4Cu–2Li–1.5Mg–0.5Mn–0.2Si–0.2Fe (2024-2Li). Wet chemical analysis of the cast alloys gave the results shown in Table I. Each of the different alloys was rapidly solidified by remelting under an argon gas atmosphere, and then melt spinning on to the outer surface of a 150 mm diameter copper wheel, using surface speeds of 8, 16 and 24 m sec^{-1}, with an argon gas ejection pressure of 35 to 40 kPa. To ensure comparability, results from each alloy were obtained from a single run of melt-spun ribbon. To investigate the decomposition behaviour of the melt-spun alloys, ribbon specimens were sealed in quartz tubes, evacuated to 10^{-5} to 10^{-6} torr, backfilled with argon gas, and then annealed at temperatures of 160, 250, 300, 400, 450 and 500° C for times ranging from 45 min to 100 h. The Al–3Cu–1.5Li–1Mg and Al–3Cu–1.5Li–1Mg–0.1Zr alloys were investigated at each annealing temperature and time, and the 2024-2Li alloy was only used to complement results from the other two alloys.

TABLE I Chemical analysis of alloy compositions (wt %)

	Cu	Li	Mg	Mn	Fe	Si	Zr
Al–Cu–Li–Mg	3.04	1.60	1.09				
Al–Cu–Li–Mg–Zr	3.06	1.61	1.09				0.11
2024-2Li	4.04	1.95	1.59	0.54	0.19	0.17	

3.2. Metallography

Metallographic examination was performed on longitudinal cross sections, and on in-plane sections of the chilled and unchilled surfaces of the different melt-spun alloys. After etching in Keller's reagent, the sections were examined in an Olympus BH optical microscope and a Jeol 35X scanning electron microscope (SEM). For examination in a Jeol 100C transmission electron microscope (TEM), thin foils were prepared from the chilled and unchilled ribbon surfaces, by grinding followed by twin jet electropolishing in a 1 : 3 nitric acid : methanol solution at about −30° C and 15 to 20 V.

3.3. Hardness measurements

The results of microhardness measurements were obtained from polished in-plane sections of the chilled surfaces of as-melt-spun and annealed ribbons in a Vickers M41 photoplan optical microscope using a pyramid objective indentor at a load of 20 g.

3.4. X-ray diffraction

A Phillips PW 1130 X-ray diffractometer was used for phase identification, with Cu $K\alpha$ X-rays at 40 kV and 20 mA, a nickel filter and a slow scanning rate of $2\theta = 1/4° \min^{-1}$. X-ray diffraction spectra were obtained from the chilled surfaces of as-melt-spun and annealed ribbons, with silicon powder sprinkled on the ribbon surface to calibrate the X-ray peak positions.

3.5 Differential scanning calorimetry (DSC)

A Dupont 1090 thermal analyser linked to a Dupont 910 DSC cell was used for thermal analysis of as-melt-spun and annealed ribbons. Individual specimens of 7 to 8 mg were heated from 100 to 560° C at a rate of 5° C $\min^{-1}$ in aluminium containers. After several trials, the maximum sampling rate of five data points per second was used to trace the fast transition peaks.

4. Results

4.1. As-melt-spun ribbons

4.1.1. Morphology

Typical examples of longitudinal cross-sections of the as-melt-spun ribbons are shown in Fig. 1. Fine-scale

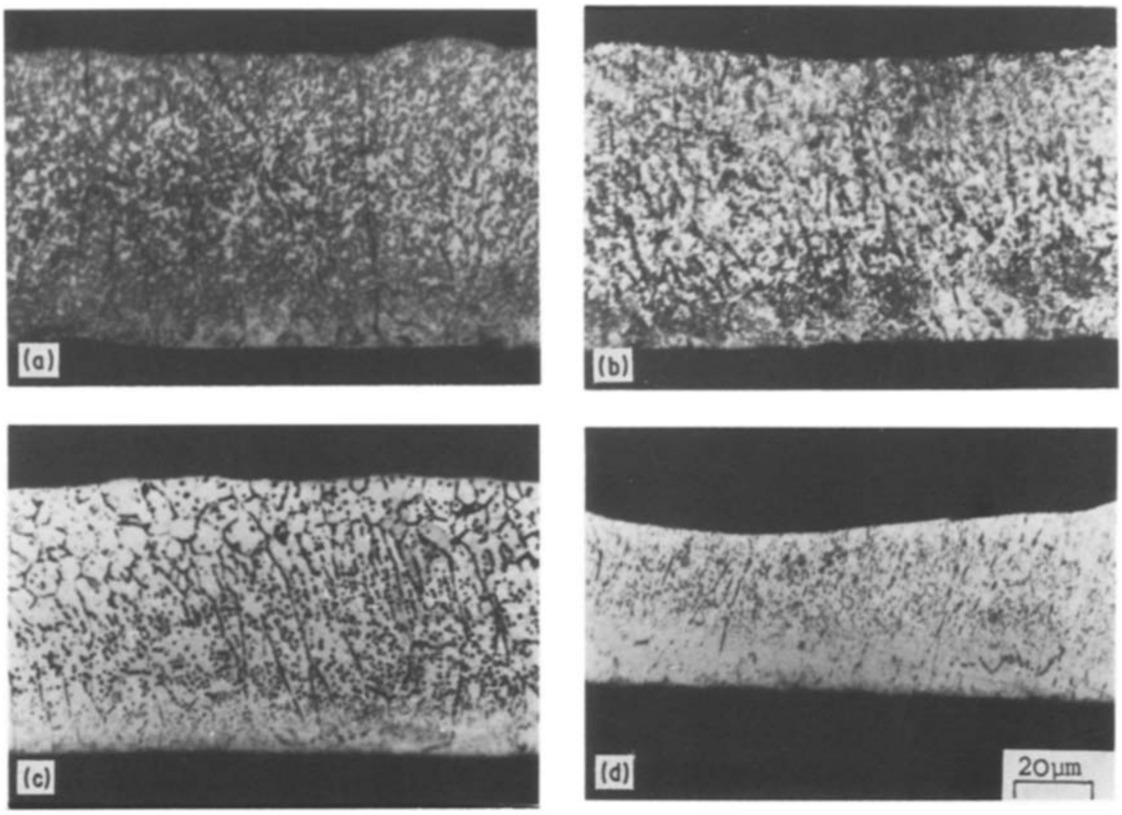

Figure 1 Optical micrographs of longitudinal through-thickness sections of as-melt-spun alloys: (a) 2024-2Li ($8\,\mathrm{m\,sec^{-1}}$), (b), (c), (d) Al–3Cu–1.5Li–1Mg (8, 16, $24\,\mathrm{m\,sec^{-1}}$, respectively). Chilled surface at bottom; unchilled surface at top.

microstructural regions which did not respond effectively to etching, were found on the chilled surfaces of the ribbons. These regions were distinguished from an etch-sensitive coarser grained structure near the unchilled surfaces. The etch-sensitive regions showed a columnar structure through the ribbon thickness, and sometimes, as shown in Fig. 1c, an equiaxed zone was also present near the unchilled surface. With increasing wheel speed, the region of fine microstructure became wider and more continuous, and the size of particles in the etch-sensitive region decreased. Typical optical microstructures of in-plane sections of chilled and unchilled surfaces are shown in Fig. 2. The microstructure of the chilled surfaces consisted of very small crystallites, as shown in Fig. 2a. On the other hand, the unchilled surfaces consisted of a coarser cell structure, with particles within the cells and at cell boundaries, as shown in Fig. 2b. Cell sizes at the chilled and unchilled surfaces were approximately 3 and $10\,\mu$m respectively.

Fig. 3 shows SEM images of chilled and unchilled surfaces of the 2024-Li ribbon melt spun at wheel speeds of 8 and $24\,\mathrm{m\,sec^{-1}}$. These micrographs were obtained by deep etching without polishing, and therefore show directly the microstructure of each surface. The unchilled surfaces in Figs 3a and c again showed a well-defined cell structure, while the chilled surfaces in Figs 3b and d consisted of very small crystallites. In Fig. 3b the small crystalline regions are separated by a coarser structure, and this type of solidification occurred more frequently at lower wheel speeds. Some evidence of this type of solidification can

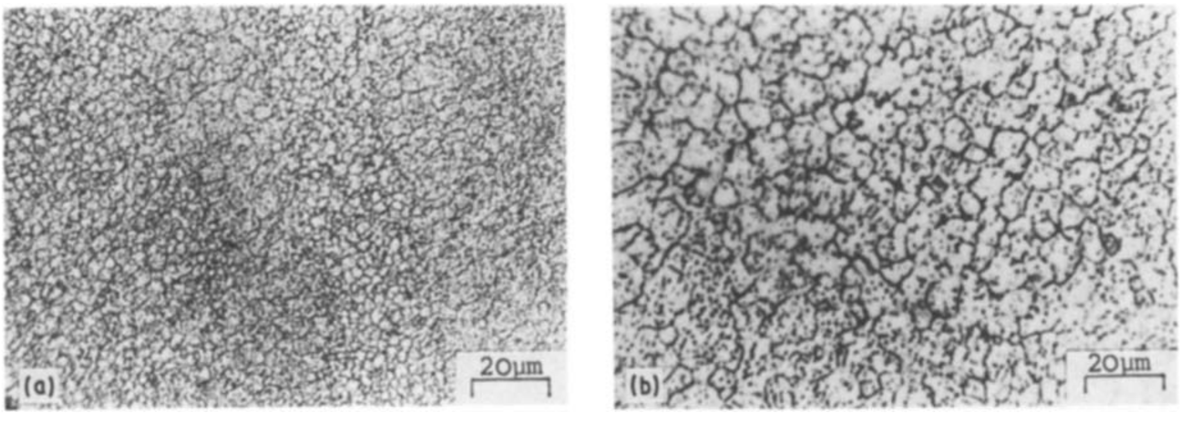

Figure 2 Optical micrographs of in-plane sections of as-melt-spun Al–3Cu–1.5Li–1Mg ($16\,\mathrm{m\,sec^{-1}}$); (a) chilled surface, (b) unchilled surface.

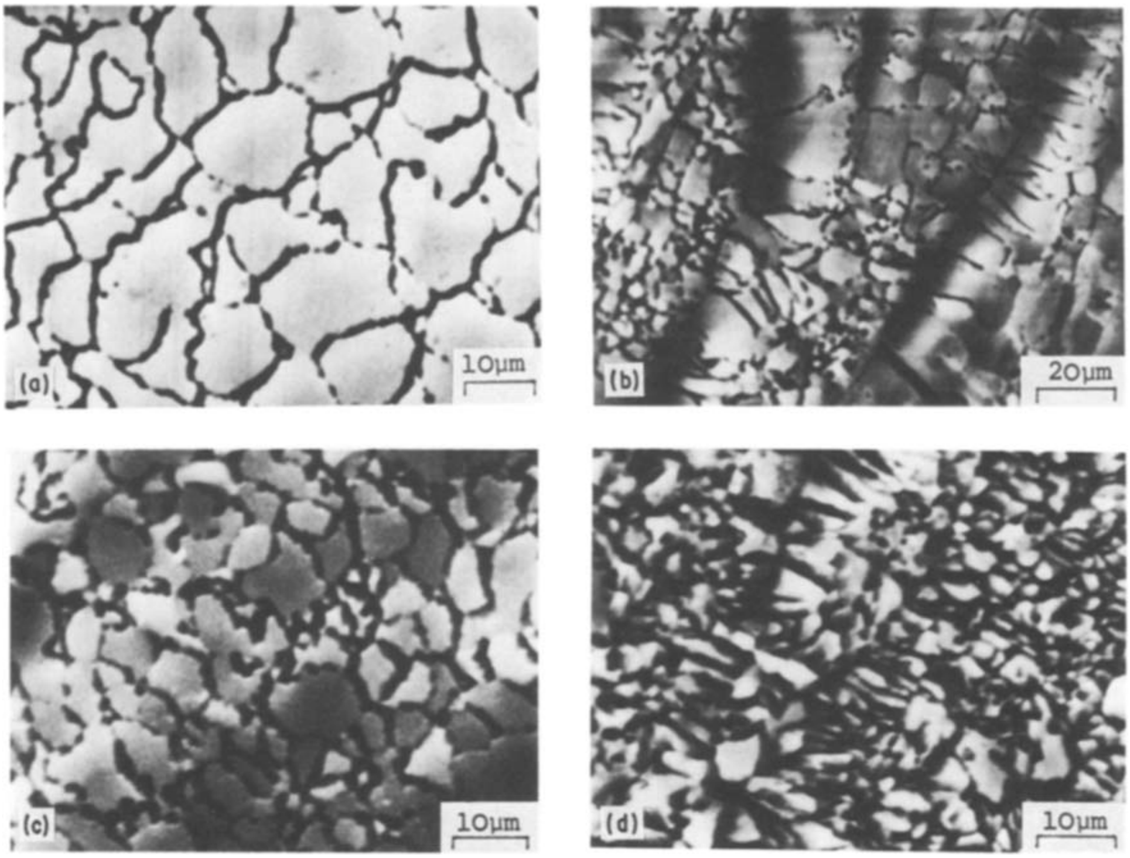

Figure 3 Scanning electron micrographs of as-melt-spun 2024-2Li; (a), (c) unchilled surfaces (8, 24 m $\sec^{-1}$, respectively), (b), (d) chilled surfaces (8, 24 m $\sec^{-1}$, respectively).

also be found in the centre of the micrograph in Fig. 3d. Cell sizes on both surfaces decreased with increasing wheel speed with typical values of approximately 7 and 15 μm at 24 and 8 m $\sec^{-1}$, respectively, on the unchilled surface.

4.1.2. TEM results

Typical TEM microstructures of chilled and unchilled regions are shown in Fig. 4. Very small particles of $< 0.1\,\mu$m diameter were found to be dispersed in the aluminium solid solution matrix near the chilled surfaces, as shown in Fig. 4a. Near the unchilled surfaces, however, coarser particles were seen inside the cells and at cell boundaries as shown in Fig. 4b. As shown in Fig. 5, the particles inside the cells were nearly spherical, with a typical mottled appearance, and were identified by electron diffraction as having an icosahedral structure. Typical five- and two-fold symmetry diffraction patterns are shown in Figs 5c to e. (The micrographs in Fig. 5 were obtained from a section approximately midway between the chilled and unchilled surfaces of the ribbon, and all subsequent transmission electron micrographs in this paper were taken from equivalent mid-plane sections.) The cell boundary particles were also found to have an icosahedral structure, as shown by the three-fold symmetry diffraction pattern and dark field image in Fig. 6. The δ' phase was also present in the as-melt-spun alloy ribbons, as shown in the diffraction pattern in Fig. 5b. However, the δ' particles could not be

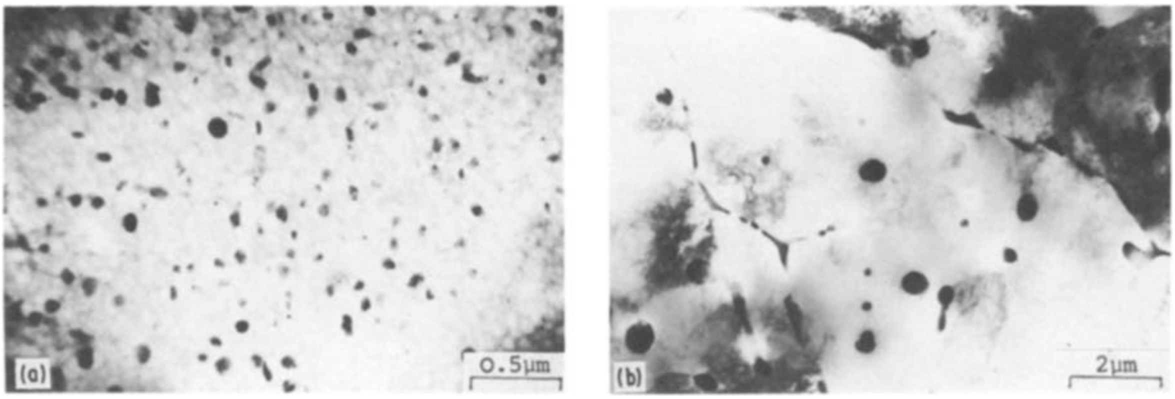

Figure 4 Transmission electron micrographs of as-melt-spun Al–3Cu–1.5Li–1Mg–0.1Zr (8 m $\sec^{-1}$); (a) chilled zone, (b) unchilled zone.

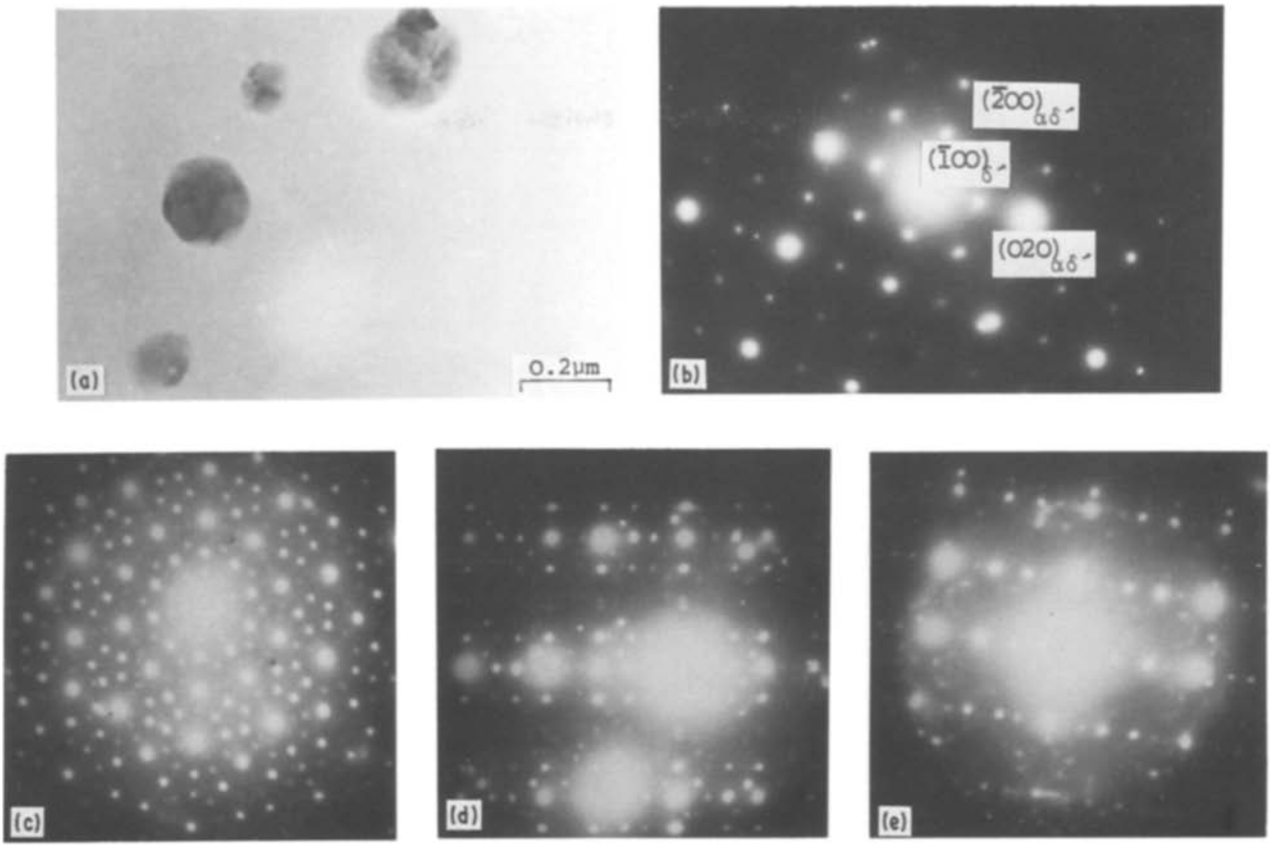

Figure 5 Transmission electron micrographs of as-melt-spun Al–3Cu–1.5Li–1Mg–0.1Zr (16 m sec^{-1}); (a) icosahedral particles inside the cells, (b) diffraction pattern of α matrix showing [0 0 1] α and δ' zone, (c), (d), (e) typical five-fold symmetry (c) and two-fold symmetry (d, e) icosahedral diffraction patterns.

imaged, because of their small size. All three alloys which were investigated contained both icosahedral and δ' phases in the as-spun condition. To study the effect of melt-spinning wheel speed on icosahedral particle size, particle diameters were measured on mid-plane sections of ribbons manufactured at wheel speeds of 8, 16 and 24 m sec^{-1} in both Al–3Cu–1.5Li–1Mg and Al–3Cu–1.5Li–1Mg–0.1Zr alloys. The results are shown in Fig. 7, with typical transmission electron micrographs in Fig. 8. As can be seen in Figs 7 and 8, the icosahedral particle size showed a strong dependence on melt-spinning wheel speed in both alloys, decreasing from approximately 0.2 to < 0.1 μm as the wheel speed increased from 8 to 24 m sec^{-1}. The as-melt-spun alloy microhardness showed a similar strong dependence on melt spinning

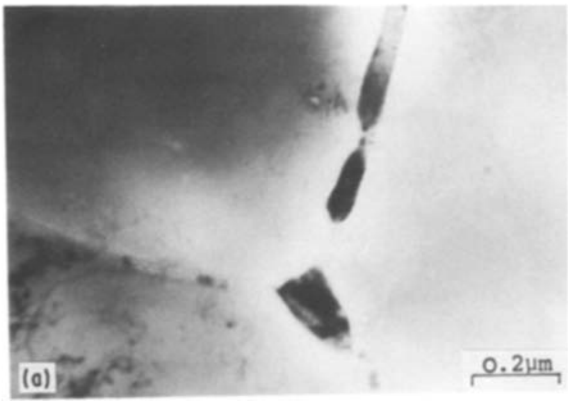

Figure 6 Transmission electron micrographs of as-melt-spun Al–3Cu–1.5Li–1Mg (8 m sec^{-1}); (a) BF image of intercellular phase, (b) DF image of (a) with three-fold symmetry icosahedral diffraction pattern (c).

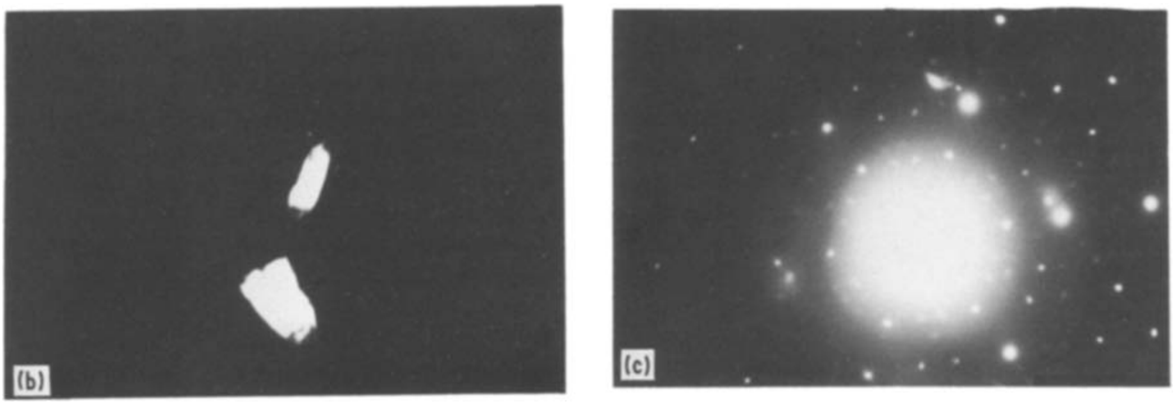

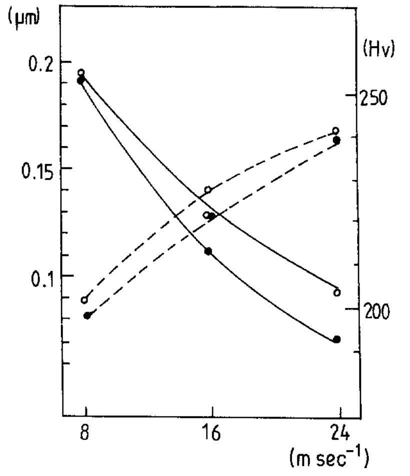

Figure 7 Variation of as-melt-spun icosahedral particle size and ribbon hardness as a function of wheel speed: (——) icosahedral particle size (– – –) ribbon hardness. (○) Al–Cu–Li–Mg–Zr. (●) Al–Cu–Li–Mg.

wheel speed, increasing from 200 to 250 Hv as the wheel speed increased from 8 to 24 m sec^{-1}, as shown in Fig. 7.

4.2. Heat-treated ribbons

4.2.1. *TEM results*

Typical microstructural changes during annealing of melt-spun Al–3Cu–1.5Li–1Mg are shown in Fig. 9. No significant difference was found in Al–3Cu–1.5Li–1Mg–0.1Zr. As shown in Fig. 9, precipitation during annealing took place in a complex way, and the phases identified after annealing for different times at the different temperatures are summarized in Table II.

TABLE II Phases identified by TEM at each stage of annealing

Temperature (° C)	Time (h)	
	5	100
160	I, δ'	I, δ' (θ', S$'$ begin to form)
250	I, θ', S$'$	I
300	I	I
400	I	I
500	I, δ' (T_1, T_2(bcc) begin to form)	δ' T_1, T_2(bcc),* two other phases

*After annealing for 15 h.
I = icosahedral phase.

An interesting point to notice is that the icosahedral phase persisted throughout annealing until finally decomposing at 500° C. The following paragraphs describe the different microstructural changes which took place during annealing at each temperature.

(a) Annealing at 160° C. After annealing for 100 h at 160° C, δ' particles which were unresolvable in the as-spun condition grew substantially, as shown by the bright- and dark-field images in Figs 10a and b. The icosahedral particles also increased in size, while retaining a near-spherical shape, as can be seen by comparing Figs 9a and 8c. A lithium-depleted zone was observed around the icosahedral particles and along grain boundaries such as shown in Figs 10a and b, indicating that a supply of lithium atoms was needed to sustain icosahedral particle growth. It was not clear whether a similar lithium-depleted zone existed around the icosahedral particles before annealing, because a dark-field image equivalent to Fig. 10b could not be obtained for the as-spun condition. The dark-field image in Fig. 10c clearly shows the typical mottled appearance and near-spherical shape of the icosahedral particles. As can be seen from Fig. 9a, other phases such as θ' and S$'$ were just beginning to form after 100 h at 160° C.

(b) Annealing at 250° C. The θ' and S$'$ phases were observed more clearly after annealing at 250° C for 5 h, as shown in Fig. 9b. These three phases were

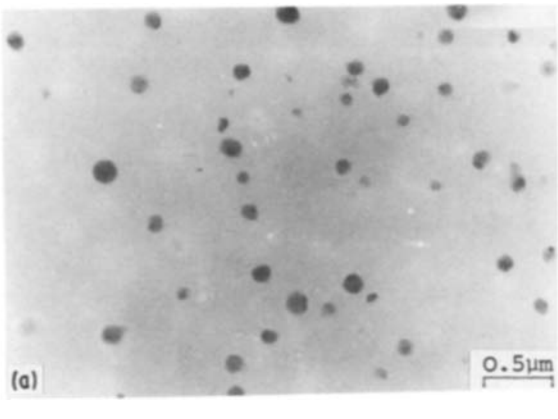

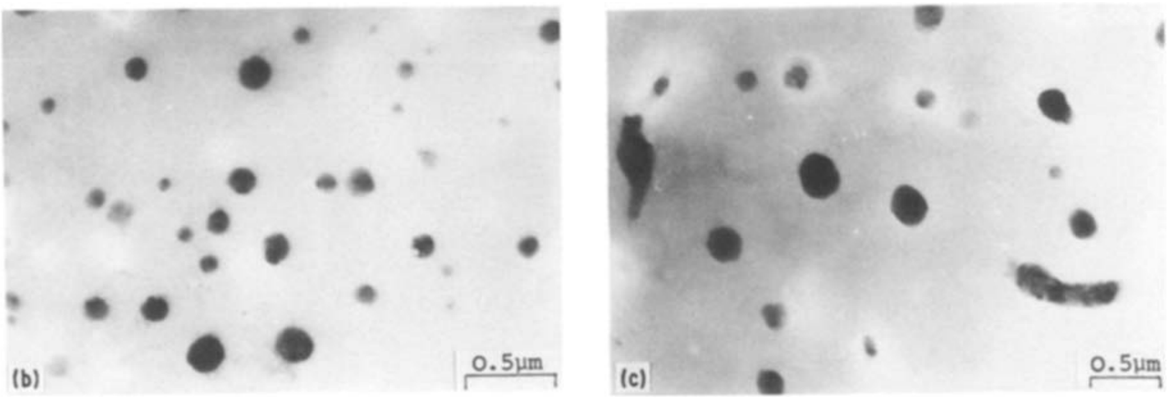

Figure 8 Variation of as-melt-spun icosahedral particle size as a function of wheel speed in Al–3Cu–1.5Li–1Mg; (a) 24 m sec^{-1}, (b) 16 m sec^{-1}, (c) 8 m sec^{-1}.

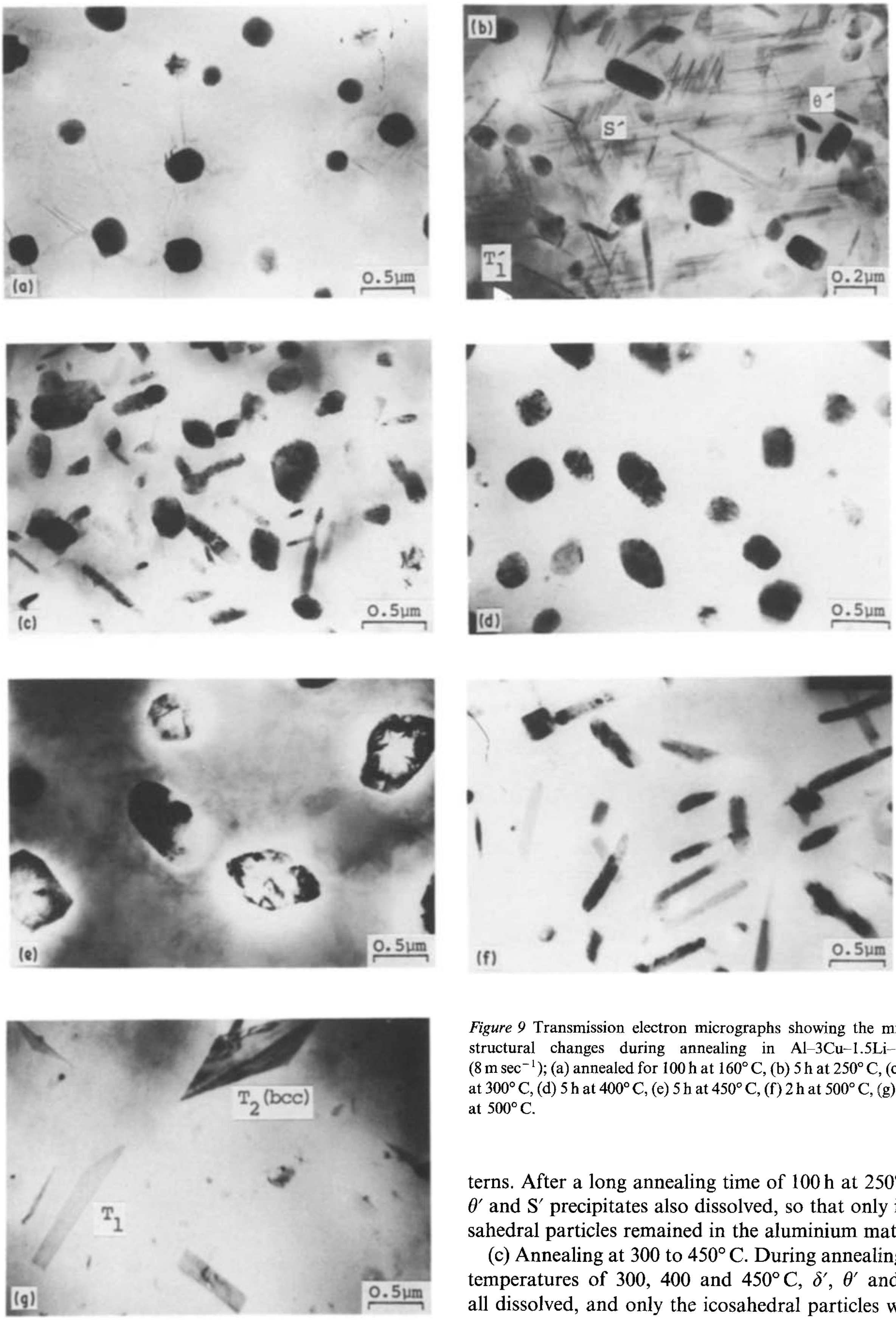

Figure 9 Transmission electron micrographs showing the microstructural changes during annealing in Al–3Cu–1.5Li–1Mg (8 m sec^{-1}); (a) annealed for 100 h at 160° C, (b) 5 h at 250° C, (c) 5 h at 300° C, (d) 5 h at 400° C, (e) 5 h at 450° C, (f) 2 h at 500° C, (g) 15 h at 500° C.

identified from their characteristic diffraction patterns and corresponding dark-field images, as shown in Fig. 11. After annealing for 5 h at 250° C, the microstructure contained particles of θ', S', and the icosahedral phase embedded in a matrix of aluminium. However, the δ' particles had dissolved and there was no evidence of δ' spots on any electron diffraction patterns. After a long annealing time of 100 h at 250° C, θ' and S' precipitates also dissolved, so that only icosahedral particles remained in the aluminium matrix.

(c) Annealing at 300 to 450° C. During annealing at temperatures of 300, 400 and 450° C, δ', θ' and S' all dissolved, and only the icosahedral particles were present, as shown in Figs 9c, d and e. As can be seen in Fig. 9, the icosahedral particles continued to grow in size during annealing, and changed morphology from near-spherical in the as-spun alloy and to various rod and faceted types after annealing above 250° C. The icosahedral particle size was therefore measured as a function of isochronal annealing in Al–3Cu–1.5Li–1Mg–0.1Zr, and isothermally in both Al–3Cu–1.5Li–1Mg and Al–3Cu–1.5Li–1Mg–0.15Zr

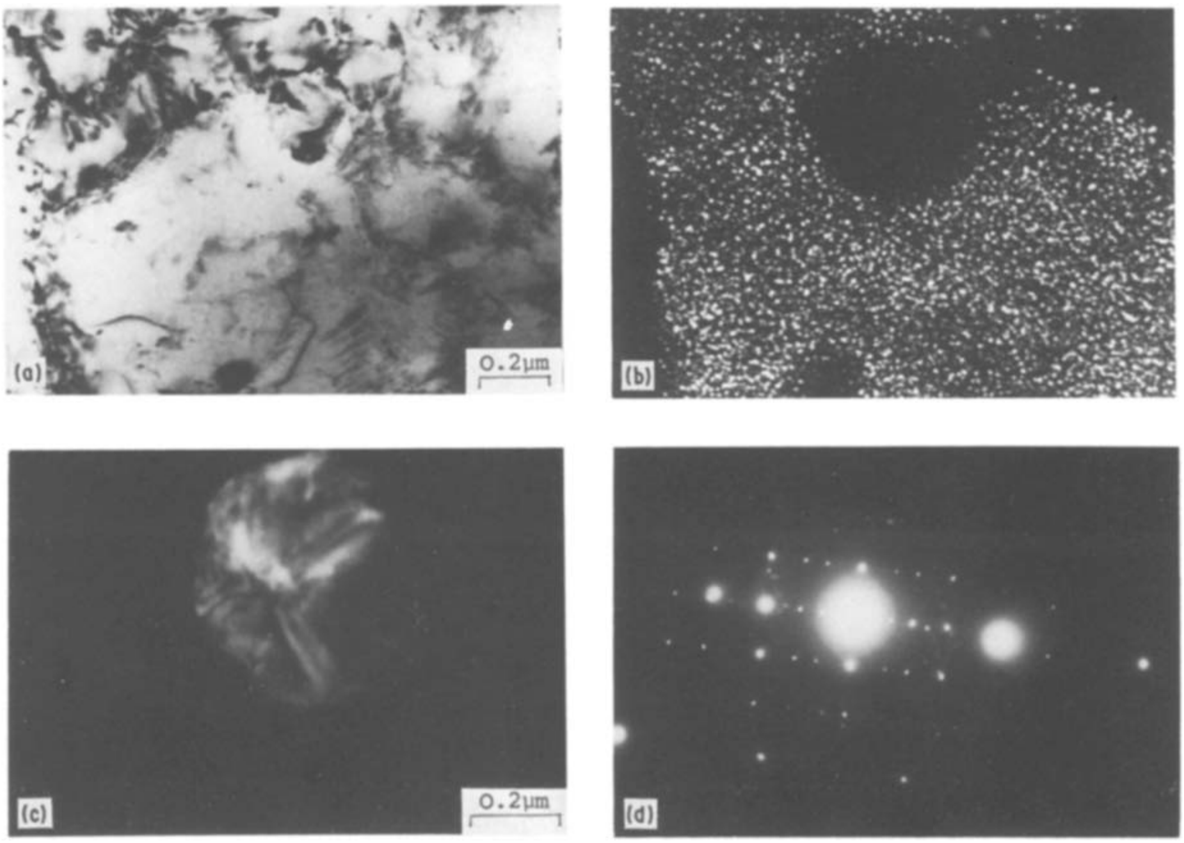

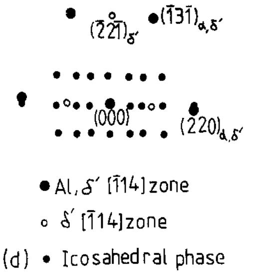

Figure 10 Transmission electron micrographs of δ′ and icosahedral particles in Al–3Cu–1.5Li–1Mg–0.1Zr annealed for 100 h at 160° C; (a) bright-field image, (b) dark-field image of δ′ precipitates, (c) dark-field image of an icosahedral particle, (d) diffraction pattern showing superimposed $[\bar{1}\,1\,4]_\alpha$, $[\bar{1}\,1\,4]_{\delta'}$, and two-fold symmetry icosahedral zones.

at 300 and 400° C. The results in Figs 12 and 13 showed a growth rate which increased sharply at the higher annealing temperatures and longer annealing times. Cell-boundary icosahedral particles grew particulary rapidly, as shown in Fig. 14.

(d) Annealing at 500° C. As shown in Fig. 9f, icosahedral particles still remained after annealing at 500° C for 2 h. After annealing for 15 h, however, the icosahedral particles dissolved, and the stable T_1 and T_2(b c c) phases precipitated, as shown in Fig. 9g. These two stable phases were identified from their characteristic diffraction patterns and corresponding bright- and dark-field images, as shown in Fig. 15. In addition to T_1 and T_2(b c c), two other phases were occasionally seen, which had the characteristic electron diffraction patterns and corresponding bright-field images shown in Fig. 16. These two phases could not be identified unambiguously, but were similar to the new phases previously reported by Ball and Lagace [32] in Al–Cu–Li–Mg alloys. The δ′ phase reappeared after annealing at 500° C, as can be seen in the electron diffraction pattern in Fig. 15a.

4.2.2. Hardness measurements

Fig. 17 shows the hardness variation in melt-spun Al–3Cu–1.5Li–1Mg and Al–3Cu–1.5Li–1Mg–0.1Zr as a function of an isochronal ageing for 5 h. There was little difference between two alloys. Hardness remained almost constant up to approximately 200° C, decreased sharply with increasing temperature over the range 200 to 400° C, and then began to increase again above approximately 400° C. After annealing at 500° C, the alloy hardness reached almost the same value as at low temperatures. Fig. 18 shows the hardness variation as a function of isothermal annealing at temperatures between 160 and 500° C. As expected from Fig. 17, high levels of hardness were obtained after annealing at 160 and 500° C, whereas low levels of hardness were obtained after annealing at 300 and 400° C.

4.2.3. X-ray diffraction results

Fig. 19 shows typical X-ray spectra from as-spun and annealed ribbons of melt-spun Al–3Cu–1.5Li–1Mg. As expected from the TEM investigation, most of the X-ray peaks were from either the aluminium matrix or the icosahedral particles. The intensities and angular positions of the icosahedral X-ray peaks remained almost constant with heat treatment up to 5 h at 500° C. As shown in Fig. 19e, however, the icosahedral phase disappeared after 15 h annealing at 500° C and the T_1 phase was detected at low intensity. Other metastable and stable precipitates were not resolved by X-ray diffraction.

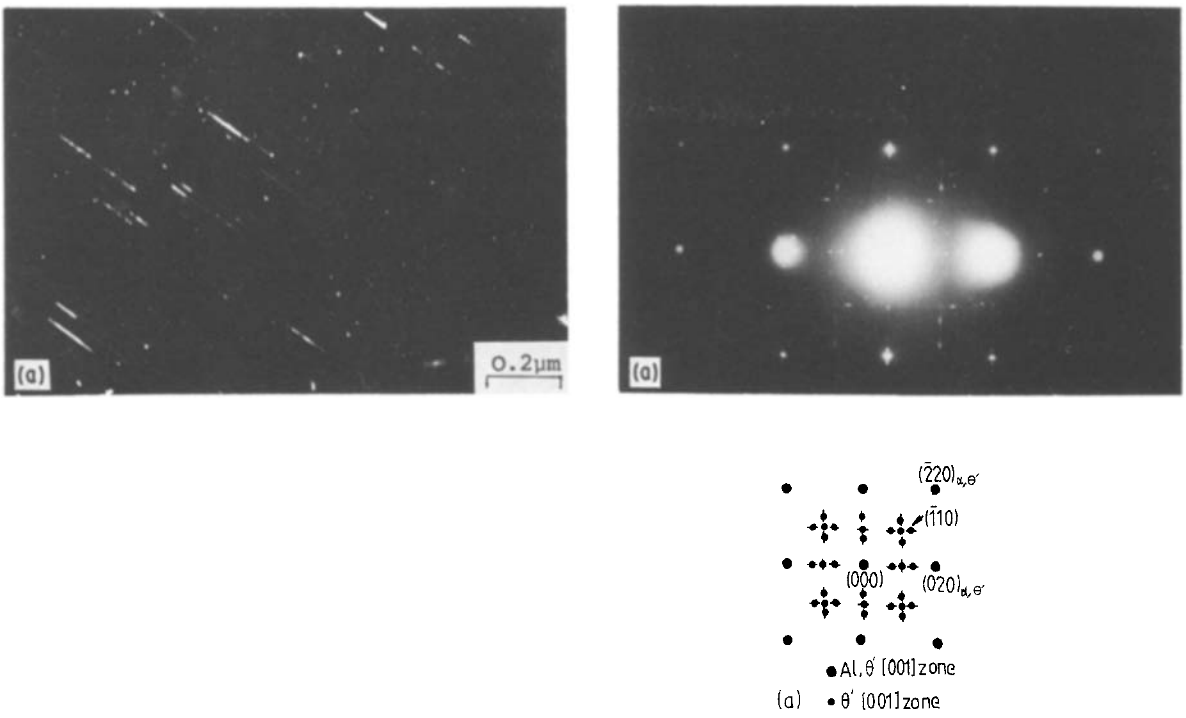

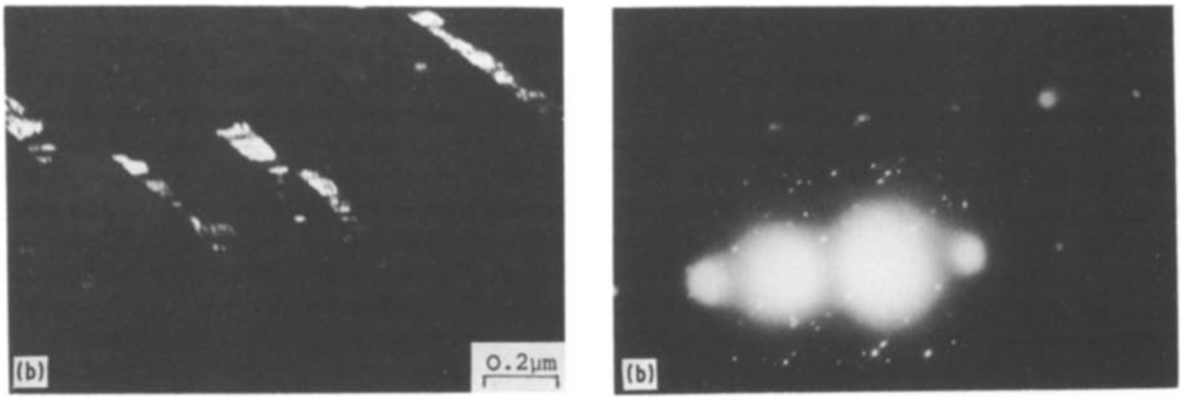

Figure 11 Transmission electron micrographs of θ′, S′, T_1' precipitates in Al–3Cu–1.5Li–1Mg annealed for 5 h at 250° C; (a) dark-field image of θ′ precipitates with corresponding diffraction pattern showing superimposed $[0\,0\,1]_\alpha$ and $[0\,0\,1]_{\theta'}$ zones, (b) dark-field image of S′ precipitates with corresponding diffraction pattern showing superimposed $[\bar{1}\,1\,2]_\alpha$ and $[1\,0\,1]_{S'}$ zones.

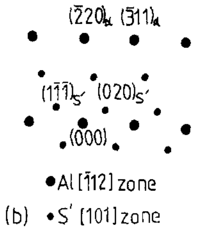

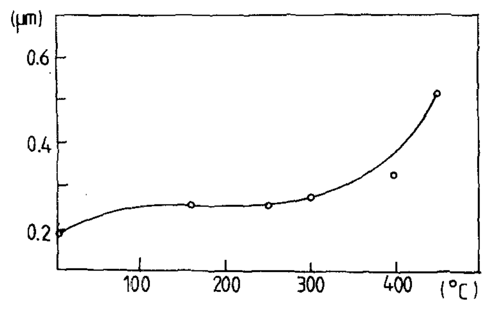

Figure 12 Icosahedral particle coarsening as a function of isochronal annealing temperature for 5 h in Al–3Cu–1.5Li–1Mg–0.1Zr (8 m sec^{-1}).

4.2.4. DSC results

Typical DSC traces are shown in Fig. 20 as a function of heat treatment. In Fig. 20, curves a and b are from the Al–3Cu–1.5Li–1Mg–0.1Zr alloy, whereas c, d and e are from the Al–3Cu–1.5Li–1Mg alloy. Both alloys again showed similar behaviour. Interestingly, DSC traces from specimens annealed at 500° C were similar to traces from as-melt-spun specimen. A total of three endothermic and three exothermic peaks were present in the DSC traces as numbered in Fig. 20a.

The two endothermic peaks 1 and 2 appeared at 120 to 160° C and 180 to 240° C, respectively, in DSC traces from as-melt-spun ribbons. Peaks 1 and 2

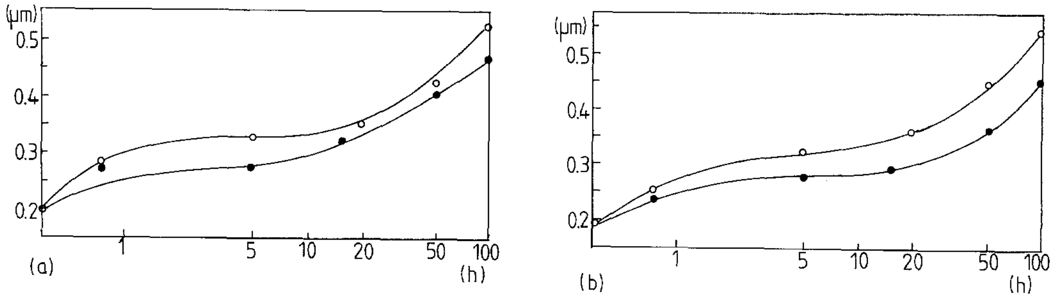

Figure 13 Icosahedral particle coarsening as a function of isothermal annealing time at (●) 300 and (○) 400° C: (a) Al–3Cu–1.5Li–1Mg, (b) Al–3Cu–1.5Li–1Mg–0.1Zr (8 m sec^{-1}).

disappeared in specimens annealed at temperatures below 500° C, and reappeared in specimens annealed at 500° C. Peaks 1 and 2 corresponded to the dissolution of G.P. zones and δ'. G.P. zones were not detected in the present TEM study, but the existence of G.P. zones in conventionally cast aluminium–lithium alloys has been suggested previously [16, 17]. Dissolution of δ' was found by TEM to take place after annealing for 5 h at 250° C, as shown in Fig. 9b, so the present TEM and DSC results both indicate a δ' solvus of approximately 250° C, in good agreement with previous reports [16].

The two exothermic peaks 3 and 4 appeared at 240 to 280° C and 300 to 340° C, respectively, in DSC traces from as-melt-spun ribbons. Peaks 3 and 4 disappeared in specimens annealed at 300 to 400° C, and reappeared in specimens annealed at 500° C. Peaks 3 and 4 were related to precipitation and dissolution of θ' and S'. As shown in Figs 9b and 11, TEM observations showed that these phases precipitated extensively after short annealing times at 250° C, and then dissolved after longer annealing times at the same temperature.

The origin of the exothermic peak 5 at 400 to 450° C was not clear. TEM observations showed icosahedral particle growth at temperatures above 300° C, and peak 5 perhaps corresponded to this icosahedral coarsening reaction. Thus, this peak was present in as-melt-spun and low-temperature annealed ribbons (Figs 20a and b), but not present after annealing above 400° C (Figs 20d and e) when most of the icosahedral phase particles had either coarsened (Fig. 20d) or decomposed (Fig. 20e).

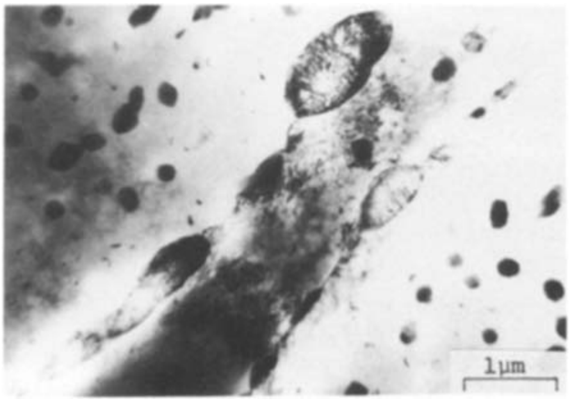

Figure 14 Transmission electron micrograph of intercellular icosahedral phase in Al–3Cu–1.5Li–1Mg–0.1Zr after annealing for 20 h at 400° C.

The very sharp endothermic peak 6 at 530° C almost certainly corresponded to the onset of melting. During relatively rapid heating in the DSC, melting presumably began before precipitation of equilibrium phases such as T_1 and T_2(b c c).

5. Discussion

5.1. As-rapidly solidified alloys

5.1.1. Grain structure and segregation

As shown in Figs 1 to 3, the microstructures of as-melt-spun ribbons of Al–Cu–Li–Mg–Zr alloys consist of columnar through-thickness cells, which increase in size from the chilled to the unchilled surface. Longitudinal cross sections in Fig. 1 show an etch-sensitive region near the unchilled surface, and a non etch-sensitive region near the chilled surface. The relative proportions of these two regions is determined by melt-spinning wheel speed, with the non-etch-sensitive fine chill zone becoming wider and more continuous with increasing wheel speed. At lower wheel speeds, a coarser microstructure is also found at the chilled surface, because of poor contact regions between the solidifying alloy and wheel surface. During melt spinning, solidification begins at each contact point with the wheel surface, forming the fine-scale non-etching microstructure in Fig. 1, but separated by a coarser dendritic microstructure [33] such as shown in Fig. 3b. Fig. 1c shows an equiaxed zone near the unchilled ribbon surface, which is not seen in other ribbons, and is probably caused by inclusions which can act as nuclei for equiaxed grains during the later stages of solidification.

5.1.2. δ' and icosahedral phase

Since Schechtman *et al.* [34] first found icosahedral point symmetry in rapidly solidified Al–10 to 14 at % Mn alloys, there have been many other reports of icosahedral phases in Al–Mn and other alloy systems. In the present study, icosahedral particles form very extensively in rapidly solidified Al–Cu–Li–Mg–Zr alloys. The icosahedral particles are found within the solidification cells as well as at cell boundaries, and probably form as a second-phase solidification reaction. The icosahedral particles have a characteristic mottled appearance, similar to that found

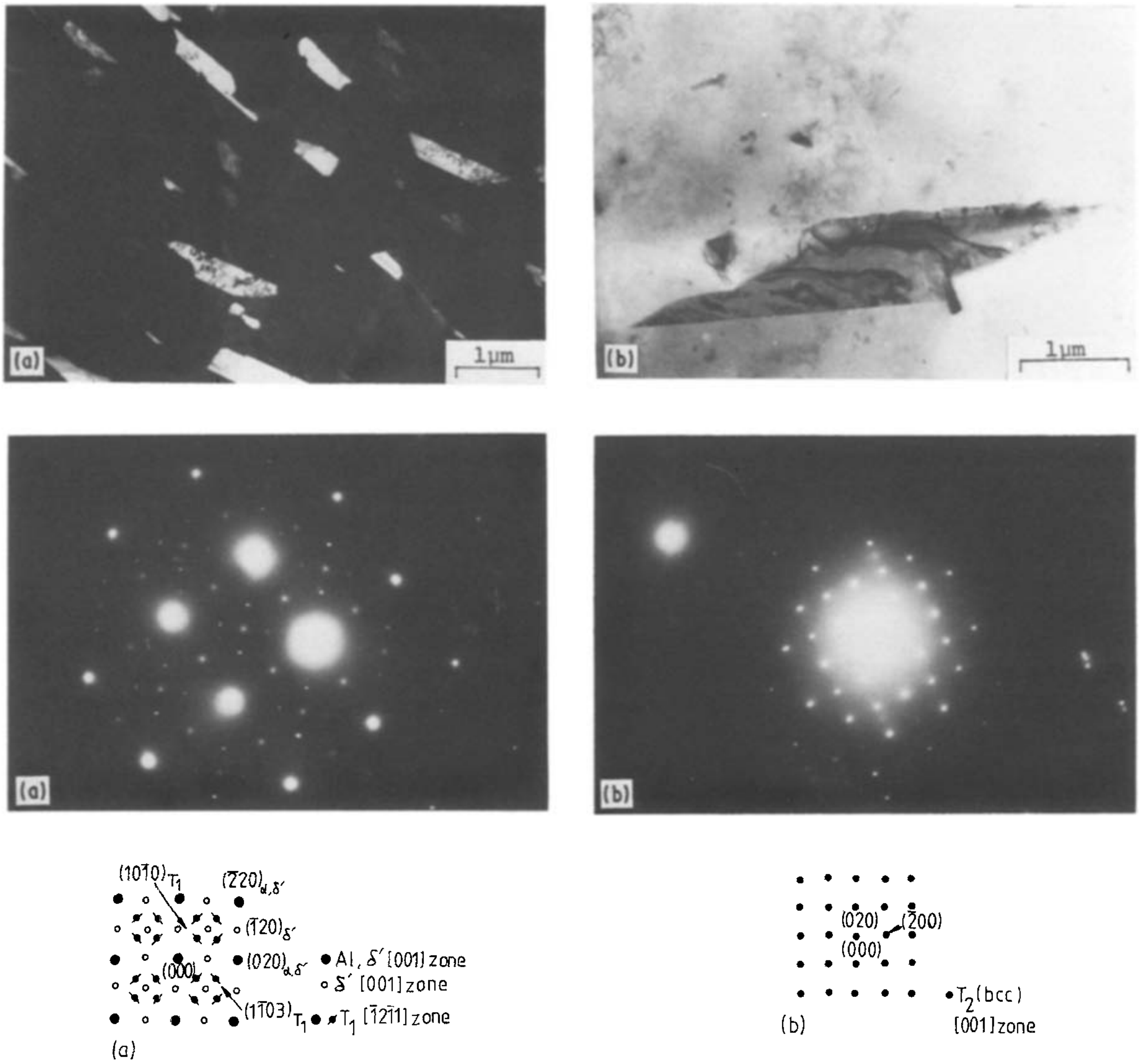

Figure 15 Transmission electron micrographs of T_1 and T_2(b c c) stable precipitates in Al–3Cu–1.5Li–1Mg annealed for 15 h at 500° C; (a) dark-field image of T_1 with corresponding diffraction pattern showing superimposed $[0\,0\,1]_\alpha$, $[0\,0\,1]_{\delta'}$ and $[\bar{1}\,2\,1\,1]_{T_1}$ zones, (b) bright-fiel image of T_2(b c c) with corresponding diffraction pattern showing $[0\,0\,1]_{T_2}$ zone.

previously in other alloy systems, but are nearly spherical in shape unlike the dendritic icosahedral particles in Al–Mn [35].

The T_2 phase has been reported to have either a b c c structure isomorphous with $Mg_{32}(Zn, Al)_{49}$ [21], or an icosahedral structure with m $\bar{3}\,\bar{5}$ point group symmetry [10, 22, 23]. The present study shows that both of these T_2 structures can form in melt-spun Al–Cu–Li–Mg–Zr. Table III shows Hardy and Silcock's diffraction results from T_2 [20], as indexed by Marcus and Elser [36], together with the present X-ray results from the annealed icosahedral particles. The similar wave vectors and diffraction intensities in Table III confirm Marcus and Elser's suggestion that the T_2

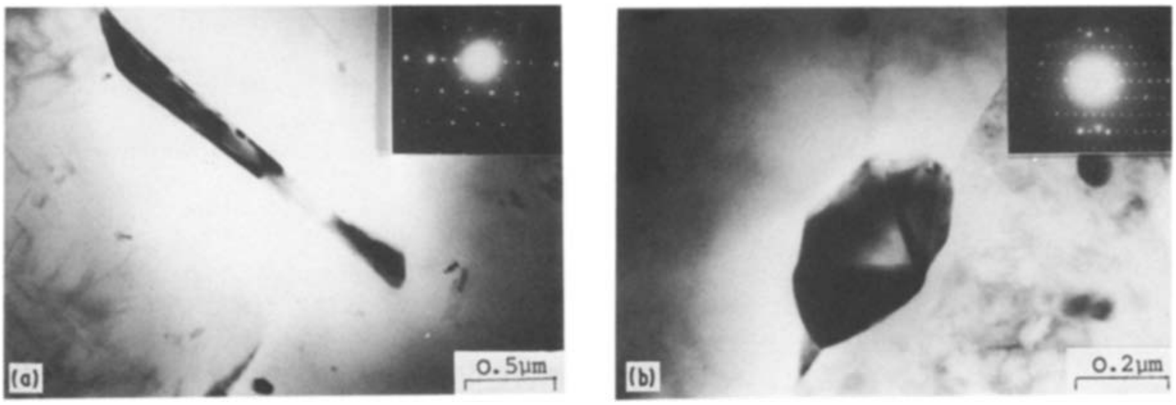

Figure 16 Transmission electron micrographs and corresponding electron diffraction patterns of precipitate particles: (a) in Al–3Cu–1.5Li–1Mg after annealing for 15 h at 500° C, (b) in 2024-2Li after annealing for 5 h at 500° C.

TABLE III Comparison of X-ray data

This study*		Hardy and Silcock [20]		Marcus and Elser [36] Indexing
q (nm^{-1})	Intensity	q (nm^{-1})	Intensity	
		10.631	W	(1 1 0 0 0 0)
		14.819	S	(1 1 0 0 0 1)
26.104	39	26.624	M	(2 1 1 1 1 1)
27.965	100	27.925	S	(2 1 0 0 1 2)
		31.260	S	†
31.645	79	31.894	MS	(2 2 0 0 1 2)
32.491	62	32.725	MW	(3 1 1 1 1 1)
‡		38.312	W	(3 2 1 0 1 2)
45.108	51	45.073	S	(3 2 0 0 2 3)
		48.407	W	(4 2 1 1 2 2)
52.886	35	52.711	MW	(4 2 1 1 2 3)
				(4 3 1 0 1 3)

*Data from the ribbon annealed at 400° C for 100 h.
†Peak corresponds to Al(2 0 0) peak [36].
‡Peak seems to be overlapped with Si peak.

phase reported by Hardy and Silcock has an icosahedral structure. The icosahedral particles therefore have a composition of approximately Al_6CuLi_3, and from Fig. 19, a quasi lattice parameter of 0.504 nm in good agreement with Cassada *et al.* (0.510 nm) [23] and Marcus and Elser (0.502 nm) [36]. In addition to the icosahedral T_2 phase particles, after annealing at 500° C, melt-spun Al–Cu–Li–Mg–Zr alloys contain a precipitate with the T_2(b c c) structure isomorphous with $Mg_{32}(Al, Zn)_{49}$, as shown in Fig. 15.

As shown in Fig. 5, very fine scale δ' precipitate particles were found to co-exist with the icosahedral particles in as-melt-spun Al–Cu–Li–Mg–Zr alloys. As mentioned above, δ' is reported to precipitate during solid state quenching from the single-phase region [13, 14], and the present results show that δ' can precipitate even during rapid solidification.

5.1.3. *Effect of wheel speed*

Microstructural variables such as cell size, icosahedral particle size, and proportion of fine non-etching chill zone, show a strong dependence on melt-spinning wheel speed. The as-spun hardness also increases with increasing wheel speed, and this is because of the decreasing cell and grain size rather than the decreasing icosahedral particle size, because the annealing studies in Figs 17 and 18 show that icosahedral particles have no significant effect on hardness.

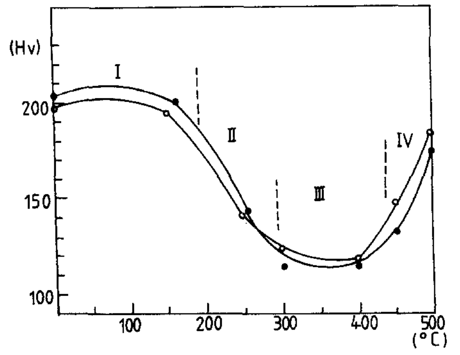

Figure 17 Variation of hardness in melt-spun alloys as a function of isochronal annealing for 5 h. (●) Al–Cu–Li–Mg–Zr, (○) Al–Cu–Li–Mg.

5.2. Precipitation and decomposition behaviour with annealing

The precipitation behaviour in rapidly solidified Al–Cu–Li–Mg–Zr alloys follows a complex sequence, which can be expressed overall as follows:

$$\alpha + \mathrm{I} + \delta' \rightarrow \alpha + \mathrm{I} + \mathrm{S}' + \theta' \rightarrow \alpha + \mathrm{I}$$
$$\rightarrow \alpha + \delta' + \mathrm{T}_1 + \mathrm{T}_2(\mathrm{bcc}) + \text{two other phases}$$

5.2.1. *G.P. zones and δ'*

The δ' phase precipitates on a very fine scale during rapid solidification, grows during annealing at 160° C, and then dissolves during annealing at 250° C. When all other metastable precipitate phases are taken into solution during annealing at 500° C, δ' reprecipitates during cooling from the annealing temperature. This is shown clearly in the TEM and DSC results in Figs 15 and 20. Because of δ' precipitation, hardness after annealing at 500° C is as high as in the as-spun alloys (Figs 17 and 18). Dissolution of δ' particles provides solute atoms for growth of the icosahedral particles. It has been reported that addition of zirconium to lithium-containing aluminium alloys leads to precipitation of δ' around coherent metastable Al_3Zr dispersoid particles [37, 38]. In the present study, however, there was no evidence of $Al_3(Li, Zr)$ precipitation, in agreement with previous observations of rapidly solidified Al–Li–Zr alloys [39]. The present DSC results suggest the existence of G.P. zones, although G.P. zones were not detected by the TEM study of the alloy microstructure. As with the δ' phase, G.P. zones precipitate during rapid solidification, dissolve above 200° C, and re-precipitate during cooling after annealing at 500° C.

5.2.2. *θ' and S′ phases*

Both the TEM and DSC results in Figs 9 and 20, are in good agreement, showing that the θ' and S′ phases precipitate and then decompose over the temperature ranges 240 to 280° C and 300 to 340° C, respectively. Dissolution of θ' and S′ provides solute atoms for growth of the icosahedral particles.

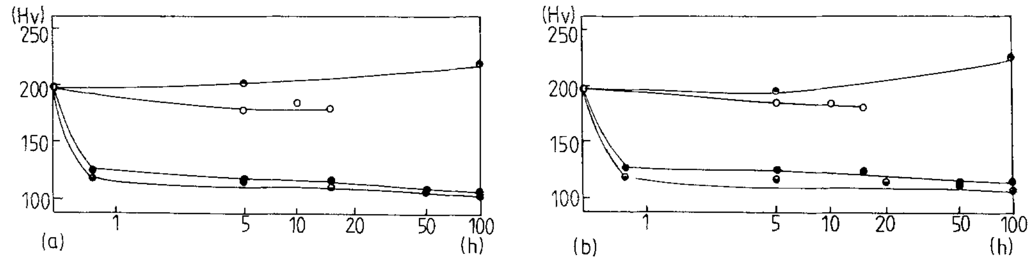

Figure 18 Variation of hardness as a function of isothermal annealing: (a) melt-spun Al–3Cu–1.5Li–1Mg alloy, (b) melt-spun Al–3Cu–1.5Li–1Mg alloy (8 m sec^{-1}). (◓) 160° C, (●) 300° C, (◒) 400° C, (○) 500° C.

5.2.3. Icosahedral phase

During annealing of rapidly solidified Al–Cu–Li–Mg–Zr alloys, as-spun spherical icosahedral particles grow at a considerable rate as shown in Figs 12 and 13, and at the same time the icosahedral particle morphology changes to various rod and faceted forms. From the TEM and X-ray diffraction results, icosahedral particles are stable at 500° C for less than 15 h. In the Al–Mn system, icosahedral particles are stable up to 400° C and then transform to $AlMn_6$ [40]. In other words, icosahedral particles in Al–Cu–Li–Mg–Zr are more stable than in Al–Mn.

5.2.4. Variation of hardness

The hardness of rapidly solidified Al–Cu–Li–Mg–Zr alloys is influenced mainly by the presence of fine scale δ'. Fig. 17 can be divided into four regions. Icosahedral and δ' particles are present in region 1, which shows the highest level of hardness. In region 2, metastable θ' and S′ have precipitated and exist together with the icosahedral particles. However, the hardness decreases as δ' dissolves. Only the icosahedral particles are present in region 3, and there is a low hardness, showing that the icosahedral particles have no significant contribution to alloy hardening. Finally in region 4, the hardness increases again because of re-precipitation of δ'.

5.2.5. Equilibrium phases

Stable T_1 and T_2(b c c) precipitate after decomposition of the icosahedral phase, together with two other phases, shown in Fig. 16. Ball and Lagace [32] have reported new stable phases in over-aged Al–Cu–Li–Mg alloys, similar to the precipitates in Fig. 16, and Kim *et al.* [41] have also reported an unidentified grain-boundary precipitate in rapidly solidified Al–Li–Cu–Mg alloy.

6. Conclusions

1. Al–Cu–Li–Mg–Zr alloys rapidly solidified by melt spinning show a columnar through-thickness,

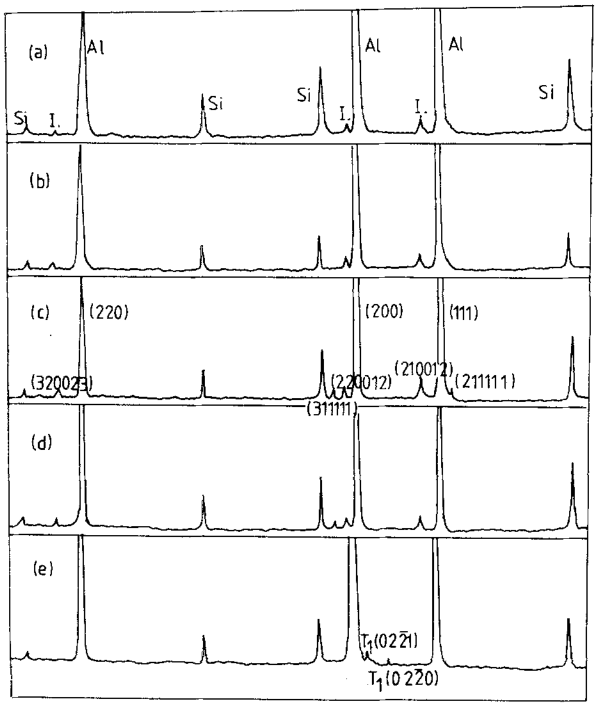

Figure 19 Typical X-ray spectra from melt-spun Al–3Cu–1.5Li–1Mg ribbons (8 m sec^{-1}): (a) as-melt-spun, (b) after annealing for 100 h at 160° C, (c) 100 h at 400° C, (d) 5 h at 500° C, (e) 15 h at 500° C.

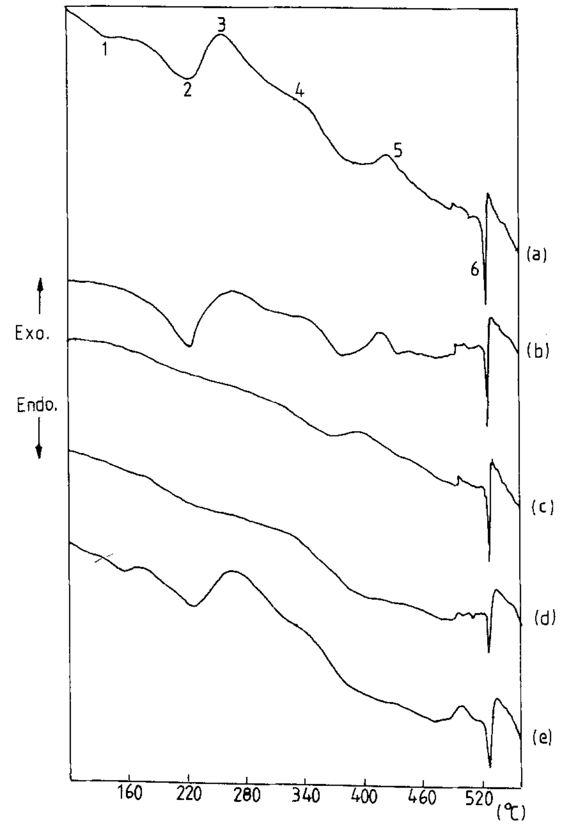

Figure 20 Typical DSC traces from melt-spun Al–3Cu–1.5Li–1Mg–0.1Zr (a, b) and Al–3Cu–1.5Li–1Mg (c, d, e): (a) as-melt-spun, (b) after annealing for 100 h at 160° C, (c) 15 h at 300° C, (d) 50 h at 400° C, (e) 15 h at 500° C.

cellular structure with second-phase particles distributed within the cells and at cell boundaries. The cell size and second-phase particle size both increase from the chilled to the unchilled melt-spun ribbon surface. These microstructural variables as well as the ribbon microhardness show a strong dependence on melt-spinning wheel speed.

2. The second-phase particles within cells and at cell boundaries have an icosahedral structure equivalent to the T_2 phase first reported by Hardy and Silcock [20]. The icosahedral particles exhibit a characteristic mottled appearance and are nearly spherical in shape. The icosahedral particle size decreases with increasing wheel speed.

3. Annealing of rapidly solidified Al–Cu–Li–Mg–Zr alloys leads to a complex precipitation sequence which can be summarized as follows:

$$\alpha + \mathrm{I} + \delta' \rightarrow \alpha + \mathrm{I} + \mathrm{S}' + \theta' \rightarrow \alpha + \mathrm{I}$$

$$\rightarrow \alpha + \delta' + \mathrm{T}_1 + \mathrm{T}_2(\mathrm{b\,c\,c}) + \text{two other phases}$$

4. The icosahedral particles coarsen progressively during annealing, especially at the higher annealing temperatures, until dissolving after approximately 5 h at 500° C.

5. Fine-scale δ' precipitates during melt spinning, grows during annealing at low temperature, and then dissolves at higher annealing temperatures below 500° C. However, δ' re-precipitates during cooling after annealing at 500° C. Because of δ' re-precipitation during cooling, the hardness of melt-spun ribbons after annealing at 500° C is as high as in the as-spun alloys.

6. During annealing at the lower temperatures, θ' and S' precipitate and then dissolve, providing solute atoms for icosahedral particle growth.

7. Stable T_1, T_2(b c c) and two other phases precipitate after decomposition of the icosahedral particles during annealing at 500° C.

8. The microhardness of rapidly solidified Al–Cu–Li–Mg–Zr alloys is influenced mainly by fine-scale δ', while the icosahedral particles have no significant effect.

Acknowledgements

We thank Professor Sir Peter Hirsch for provision of laboratory facilities, and one of us (D. H. Kim) gratefully acknowledges the financial support of the British Council.

References

1. DONALD WEBSTER, *Met. Prog.* April (1984) 33.
2. D. M. NASER, *Light Met.* December (1984) 15.
3. DONALD D. GOEHLER, *Met. Prog.* March (1978) 38.
4. H. F. de JONG, *Aluminium* **60** (1984) 673.
5. E. A. STARKE and T. H. SANDERS, *J. Metals* August (1981) 24.
6. J. A. WERT and J. B. LUMSDEN, *Scripta Metall.* **19** (1985) 205.
7. B. NOBLE, S. J. HARRIS and K. DINSDALE, *Met. Sci.* **16** (1982) September, 425.
8. ERHARD HORNBOGEN and KARL-HEINZ EUN GAHR, *Metallography* **8** (1975) 181.
9. P. J. GREGSON and H. M. FLOWER, *Acta Metall.* **33** (1985) 527.
10. P. MEYER and B. DUBOST, in "Aluminium-Lithium Alloys III", edited by C. Baker *et al.*, (The Institute of Metals, London, 1986) p. 37.
11. C. J. PEEL, B. EVANS and D. McDARMAID, in "Aluminium-Lithium Alloys III", edited by C. Baker *et al.*, (The Institute of Metals, London, 1986), p. 26.
12. D. B. WILLIAMS and J. W. EDINGTON, *Met Sci.* **9** (1975) 529.
13. MINORU FURUAWA, YASUHIRO MIURA and MINORU NEMOTO, *Trans. Jpn Inst. Met.* **26** (1985) 414.
14. B. NOBLE and G. E. THOMSON, *Met. Sci. J.* **5** (1971) 114.
15. J. M. SILCOCK, *J. Inst. Met.* **88** (1959–1960) 357.
16. RYOICHI NOZATO and GENJI NAKAI, *Trans. Jpn Inst. Met.* **18** (1977) 679.
17. J. M. PAPAZIAN, C. SIGLI and J. M. SANCHEZ, *Scripta Metall.* **20** (1986) 201.
18. W. R. D. JONES and P. P. DAS, *J. Inst. Met.* **87** (1958–1959) 1338.
19. T. H. SANDERS and E. A. STARKE, in "Aluminium-Lithium Alloys II", edited by T. H. Sanders and E. A. Starke (The Metallurgy Society of AIME Warrendale, Pennsylvania, 1984) p. 447.
20. H. K. HARDY and J. M. SILCOCK, *J. Inst. Met.* **84** (1955–1956) 423.
21. E. E. CHERKASHIN, P. I. KRIPYAKEVICH and G. I. OLEKSIV, *Kristallografiya*, **8** (1963) 846.
22. J. M. GALBRAITH, M. H. TOSTEN and P. R. HOWELL, *J. Mater. Sci.* **22** (1987) 27.
23. W. A. CASSADA, G. J. SHIFLET and POON, *Phys. Rev. Lett.* **56** (1986) 2276.
24. BALL LLOYD, *Scripta Metall.* **19** (1985) 1065.
25. DO H. KIM, Y. W. KIM, K. H. OH and HO I. LEE, in "Proceedings of the Korean–Japan symposium on rapid solidification processing", October 1986, Korea Advanced Institute of Science and Technology.
26. H. SUZUKI, M. KANNO and N. HAYASHI, *J. Jpn Inst. Light. Met.* **32** (1982) 88.
27. R. J. RIOJA and E. A. LUDWICZAK: in "Aluminium-Lithium Alloys III", edited by C. Baker *et al.* (The Institute of Metals, London, 1986) p. 471.
28. J. C. HUANG and A. J. ARDELL: in "Aluminium-Lithium Alloys III", edited by C. Baker *et al.* (The Institute of Metals, London, 1986) p. 455.
29. *Idem, Mater. Sci. Technol.* **3** (1987) 176.
30. W. A. CASSADA, G. J. SHIFLET and E. A. STARKE, *Script. Metall.* **21** (1987) 387.
31. H. M. FLOWER and P. J. GREGSON, *Mater. Sci. Technol.* **3** (1987) 81.
32. M. D. BALL and H. LAGACE, in "Aluminium-Lithium Alloys III", edited by C. Baker *et al.* (The Institute of Metals, London, 1986) p. 555.
33. Y. R. MAHAJAN, YOUNG WON KIM and F. H. FRORES, *J. Mater. Sci.* **22** (1987) 202.
34. D. SHECHTMAN, I. BLECH, D. GRATIS and J. W. CAHN, *Phys. Rev. Lett.* **53** (1984) 1951.
35. F. H. SAMUEL, A. M. SAMUEL, A. de JONCKERE and F. GERIN, *Met. Trans.* **17A** (1986) 1671.
36. MATTHEW A. MARCUS and VEIT ELSER, *Phil. Mag. B* **54** (1984) L101.
37. F. W. GAYLE and J. B. VANDER SANDE, in "Aluminium–Lithium Alloys III", edited by C. Baker *et al.* (The Institute of Metals, London, 1986) p. 376.
38. P. L. MARKIN and B. RALPH, *J. Mater. Sci.* **19** (1984) 3835.
39. NAK J. KIM and S. K. DAS, *Script. Metall.* **20** (1986) 1107.
40. D. SHECHTMAN and I. A. BLECH, *Met. Trans.* **16A** (1985) 1005.
41. N. J. KIM, D. J. SKINNER, K. OKAZAKZ and C. M. ADAM: in "Aluminium-Lithium Alloys III", edited by C. Baker *et al.* (The Institute of Metals, London, 1986) p. 780.

Received 11 June
and accepted 27 August 1987